VNU Journal of Science: Natural Sciences and Technology
Journal homepage: https://js.vnu.edu.vn/NST

Original Article

Synthesis of $MgFe_2O_4/WO_3$ Photocatalyst for Enhanced Removal of Methylene Blue from Water

Nguyen Khanh Huyen[1], Le Thu Hien[2], Le Quynh Anh[3], Tran Dinh Trinh[2,*]

[1]*Vietnam National Institute of Occupational Safety and Health, 99 Tran Quoc Toan, Cua Nam, Hanoi, Vietnam*
[2]*VNU University of Science, 334 Nguyen Trai, Thanh Xuan, Hanoi, Vietnam*
[3]*Military Institute for Chemical and Environmental Engineering, An Khanh, Hanoi, Vietnam*

Received 04th July 2025
Revised 12th March 2026; Accepted 20th March 2026

Abstract: In this study, a series of photocatalytic materials based on $MgFe_2O_4$ and WO_3 semiconductors with various $MgFe_2O_4/WO_3$ mass ratios (1:4), (1:3), (1:2), (2:1), (3:1), and (4:1) were successfully synthesized using hydrothermal method under mild conditions. The results showed that all synthesized composites exhibited visible light absorption, with band gap energies ranging from 1.92 eV to 2.06 eV. The coupling of $MgFe_2O_4$ with WO_3 significantly enhanced photocatalytic performance by effectively suppressing the recombination of photogenerated charge carriers. Among the produced composites, $MgFe_2O_4/WO_3$ (3:1) material demonstrated the most efficient charge separation, leading to excellent degradation efficiencies regarding the degradation of Methylene Blue (MB) organic dye in water. $MgFe_2O_4/WO_3$ (3:1) photocatalyst presented a MB degradation efficiency of bout 81%, corresponding to 1.64 times higher than that of pure $MgFe_2O_4$ and 2.67 times greater than that of WO_3. These results suggest that the synergy between $MgFe_2O_4$ and WO_3 effectively reduces the recombination rate of charge carriers, thereby improving the photocatalytic degradation of organic pollutants. The degradation of MB followed the pseudo-second-order kinetics model, with R^2 within the range of 0.9769 - 0.9987 while $HO^{\bullet}$ and $O_2^{\bullet-}$ were main reactive species responsible for MB degradation process. This finding highlights the potential use of $MgFe_2O_4/WO_3$ photocatalysts for wastewater treatment application.

Keywords: Organic dyes, visible-light driven photocatalyst, water treatment, kinetics, enhanced photocatalytic performance.

1. Introduction

Dyes are widely used in various industries such as paper, printing, plastics, and particularly in the textile dyeing sector. Among them, Methylene Blue (MB) is one of the most commonly used dyes across multiple industrial applications and is recognized as one of the most prominent water pollutants [1]. Each year, a substantial amount of MB is employed as a coloring agent for paper, silk, and cotton

* Corresponding author.
E-mail address: trinhtd@vnu.edu.vn

https://doi.org/10.25073/2588-1140/vnunst.5915

materials [2], resulting in significant quantities of excessive MB being discharged into the environment. However, the release of untreated MB can pose serious risks to human health, including symptoms such as nausea, cyanosis, rapid heartbeat, and jaundice [3, 4]. Therefore, it is essential to implement effective treatment processes prior to discharge of MB into the environment to minimize its harmful impacts.

Currently, numerous studies have explored various methods for the treatment of organic dyes, including adsorption, Fenton oxidation process, photocatalysis, and persulfate activation [5, 6]. Among these methods, photocatalysis stands out due to its remarkable advantages, including high efficiency, low energy consumption, environmental friendliness, and non-toxicity [7, 8]. Moreover, photocatalysis has demonstrated excellent efficiency in degrading organic compounds into harmless end products such as CO_2 and H_2O, making it a highly promising approach for the removal of organic pollutants from wastewater [8]. However, some challenging issues related to the visible light driven photocatalyst link with i) The recombination rate of charge carriers; and ii) The generation of ineffective electrons and holes , which could not generate radicals [5, 7, 14]. To fully optimize the catalyst's effectiveness, it is essential to develop an appropriate photocatalytic system capable of complete degrading these contaminants.

$MgFe_2O_4$ is an n-type magnetic semiconductor that is free of heavy metals and exhibits high chemical stability [10, 11]. With a band gap energy ranging from 1.9 to 2.3 eV, $MgFe_2O_4$ can effectively absorb visible light and has been widely applied in water treatment using photocatalysis [11, 12]. However, $MgFe_2O_4$ primarily reduces O_2 to generate superoxide radicals ($O_2^{\bullet-}$), but lacks the ability to oxidize water to form hydroxyl radicals ($HO^{\bullet}$), which limits its photocatalytic efficiency. Therefore, numerous studies have focused on coupling $MgFe_2O_4$ with other materials to simultaneously utilize both the conduction band (CB) and valence band (VB), thereby enhancing overall photocatalytic performance [13]. Tungsten trioxide (WO_3) possesses a suitable band gap (~2.7 eV), high stability, and strong oxidative potential, making it widely studied for the photocatalytic degradation of organic pollutants [14, 15]. However, its CB potential is not sufficiently negative to facilitate the reduction reaction required for generating superoxide radicals ($O_2^{\bullet}$), which limits its catalytic activity [16]. Therefore, WO_3 is often combined with other semiconductors to better utilize its redox capabilities and to suppress the recombination of photogenerated e^-/h^+ pairs [16, 17]. The combination WO_3 and another semiconductor would create a heterojunction which not only make use of valence band (VB) of WO_3 and conduction band (CB) of the combined semiconductor, but also benefit from the restriction of charge carrier recombination rate. Inspired by that principle, the current study focuses on the designing and producing $MgFe_2O_4/WO_3$ heterojunction enhance photocatalytic performance by suppressing electron–hole recombination and simultaneously utilizing both oxidation (h^+) and reduction (e^-) processes to generate $O_2^{\bullet-}$ and $HO^{\bullet}$ radicals, thereby enabling efficient degradation of MB. In addition, this research aims to make use of the magnetism of $MgFe_2O_4$ nanoparticles to facilitate the recovery of $MgFe_2O_4/WO_3$ photocatalyst after each treatment process. The influence of pollutant concentration on the degradation process was comprehensively investigated. In addition, the reaction kinetics were thoroughly evaluated.

2. Experimental

2.1. Chemicals

Hydrochloric acid (37%), $FeCl_3.6H_2O$ (98%), $MgCl_2.6H_2O$ (99%), $Na_2WO_4{\cdot}2H_2O$ (99%), L-ascorbic acid (99%) were purchased from Sigma Aldrich. NaOH (> 96%), CH_3CH_2OH (99.7%), MB (98.5%) were from Xilong Chemical, China. All chemicals were of analytical grade, and directly used without further purification.

2.2. Synthesis of Materials

2.2.1. Synthesis of $MgFe_2O_4$

5.406 g of $FeCl_3.6H_2O$ and 2.033 g of $MgCl_2.6H_2O$ were dissolved in 100 mL of deionized (DI) water under vigorous stirring. A 5 M NaOH solution was then added dropwise to the mixture, followed by heating at 90 °C for 2 hours. The resulting precipitate was thoroughly washed with 90% ethanol and DI water until pH 7.0. The product was subsequently dried under vacuum at 60 °C for 6 hours, then ground into a fine powder and calcined at 900 °C for 3 hours to yield $MgFe_2O_4$ [18].

2.2.2. Synthesis of WO_3

5 g of $Na_2WO_4{\cdot}2H_2O$ were completely dissolved in 200 mL of DI water under continuous magnetic stirring. Subsequently, a 0.5 M HCl solution was added dropwise until a yellow precipitate of tungstic acid formed, and the mixture was stirred for an additional 2 hour. The resulting precipitate was washed several times with DI water and 90% ethanol, then dried at 100 °C, grounded into fine powders, and calcined at 600 °C for 2 hours to obtain WO_3 [19].

2.2.3. Synthesis of $MgFe_2O_4/WO_3$

A predetermined amount of $MgFe_2O_4$ and WO_3 (e.g., 0.75 g of $MgFe_2O_4$ and 0.25 g of WO_3 for 3:1 ratio) was dispersed in 50 mL of ethylene glycol to facilitate the dispersion of $MgFe_2O_4$ and WO_3 nanoparticles in solution, and form a homogeneous suspension. The mixture was then subjected to hydrothermal treatment at 125 °C for 5 hours. The resulting product was washed with DI water and 90% ethanol, followed by drying at 60 °C for 12 hours to obtain the $MgFe_2O_4/WO_3$ composites [20]

2.3. Material Characterization

X-ray diffraction (XRD), Energy Dispersive X-ray (EDX) - Mapping, Scanning Electron Microscopy (SEM), Photoluminescence spectroscopy (PL), UV–Vis diffuse reflectance spectroscopy (UV-Vis DRS) and Fourier Transform Infrared Spectroscopy (FT-IR) measurement methods were deployed to characterize the as-produce catalysts. Detailed analytical procedure for each method was presented in our previous reports [5, 7, 9]. Briefly, XRD was conducted by using a model Miniflex 600, Rigaku, Japan; SEM/EDX-mapping was performed on a SEM model Hitachi TM4000 coupled with an EDX model AZtec-Energy, Oxford, UK. PL, and UV-Vis DRS were performed on PL model FluoroMax®, Horiba, Japan while the other was conducted using a UV-Vis spectrometry, model UH4150, Hitachi, Japan. FT-IR measurement was carried out with the aid of a FT-IR model 4600, Jasco, Japan. Point of zero charges (pH_{pzc}) of the material in solutions was performed by using drift method as presented previously [21, 22].

2.4. Experiments of the Pollutant Degradation

The degradation of MB (10 mg/L) was carried out by adding 0.1 g of photocatalyst into 200 mL of the dye solution. The suspension was stirred in the dark for 30 min to allow partial adsorption of the studied dye onto the catalyst's surface, followed by illumination using a 20 W compact fluorescent lamp (3000–6000 lumens), located at 20 cm from the reaction mixture. At 30-min intervals, 3 mL of the solution were withdrawn, filtered through a 0.45 µm membrane, and analyzed for residual MB concentration using a UV-Vis spectrophotometer (model UH5300, Hitachi) at a wave length of 664 nm. The effect of dye concentration (5–20 mg/L) was also investigated. The degradation efficiency was calculated using the following equation:

$$E(\%) = \frac{(C_0 - C_t)}{C_0}.100$$

where C_0 and C_t represent the initial dye concentration and the concentration at time t (min), respectively.

3. Results and Discussion

3.1. Structural Properties of the Produced Materials

The XRD patterns of $MgFe_2O_4$, WO_3, and $MgFe_2O_4/WO_3$ composites are presented in

Figure 1a–b. The diffraction peaks at 2θ = 30.34°, 35.66°, 43.26°, 53.52°, 57.23°, and 62.63° correspond to the (220), (311), (400), (422), and (440) planes of $MgFe_2O_4$ [20]. Meanwhile, the peaks at 2θ = 23.05°, 23.57°, 24.43°, 26.54°, 28.66°, 33.21°, 34.26°, 35.64°, 41.67°, 47.28°, 48.23°, 50.03°, 55.96°, and 62.41° are indexed to the (002), (020), (200), (120), (112), (022), (202), (122), (222), (004), (040), (140), (420), and (340) planes, which are characteristic of WO_3 [22]. In the six $MgFe_2O_4/WO_3$ composites with varying mass ratios, the XRD spectra exhibit peaks corresponding to both $MgFe_2O_4$ and WO_3 crystals, with changes in intensity reflecting the $MgFe_2O_4$ and WO_3 ratios. These results confirm the successful formation of $MgFe_2O_4/WO_3$ composites with high purity and well-defined crystalline structure.

Figure 1c–d display the UV-Vis DRS spectra of the produced materials in the 300-800 nm range, confirming their high ability to absorb visible light. Based on the Tauc plots (Figure 1e–f), the band gap energies (Eg) of $MgFe_2O_4$ and WO_3 were determined to be 1.87 eV and 2.71 eV, respectively, while the $MgFe_2O_4/WO_3$ composites exhibited Eg values ranging from 1.92 to 2.06 eV.

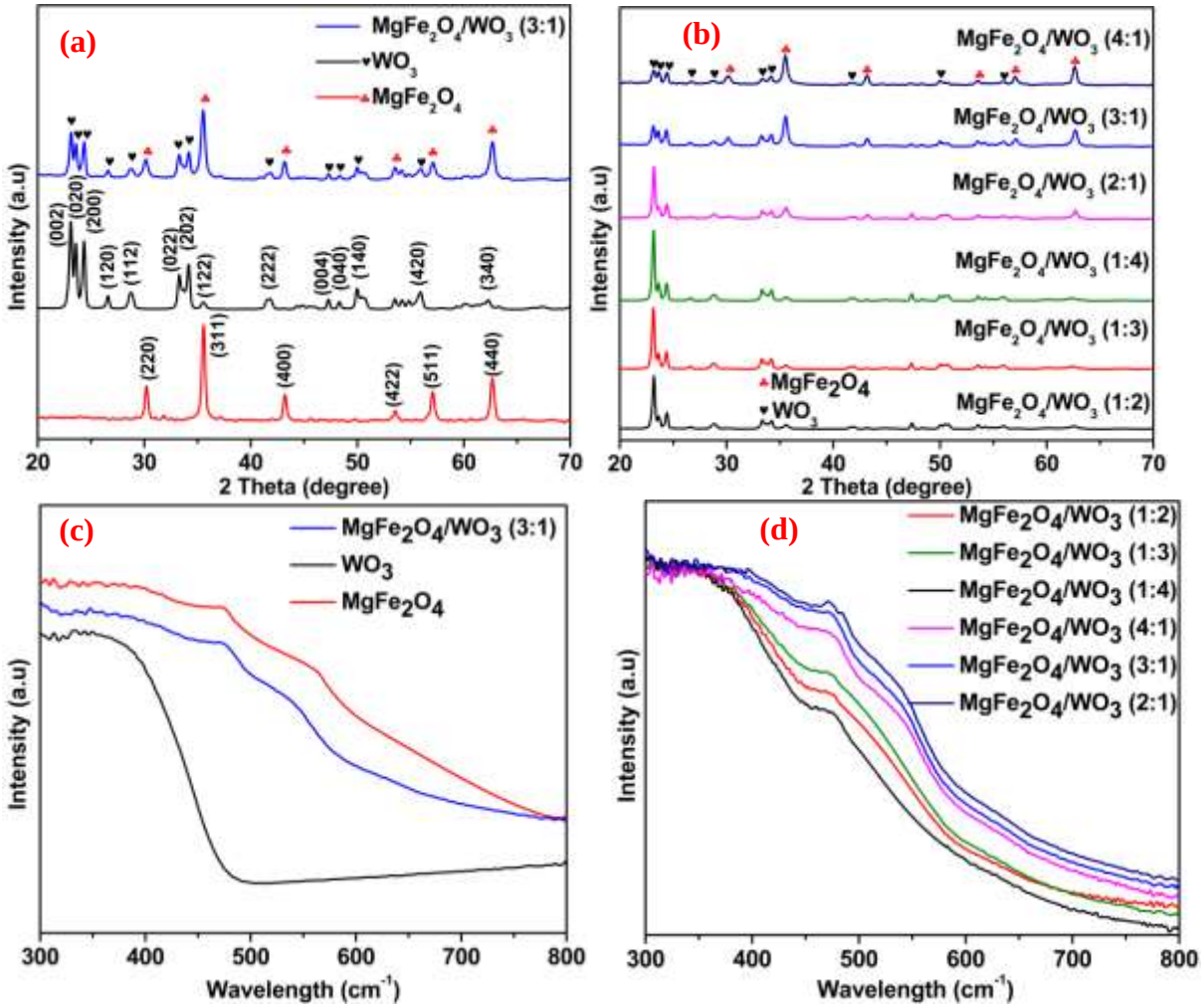

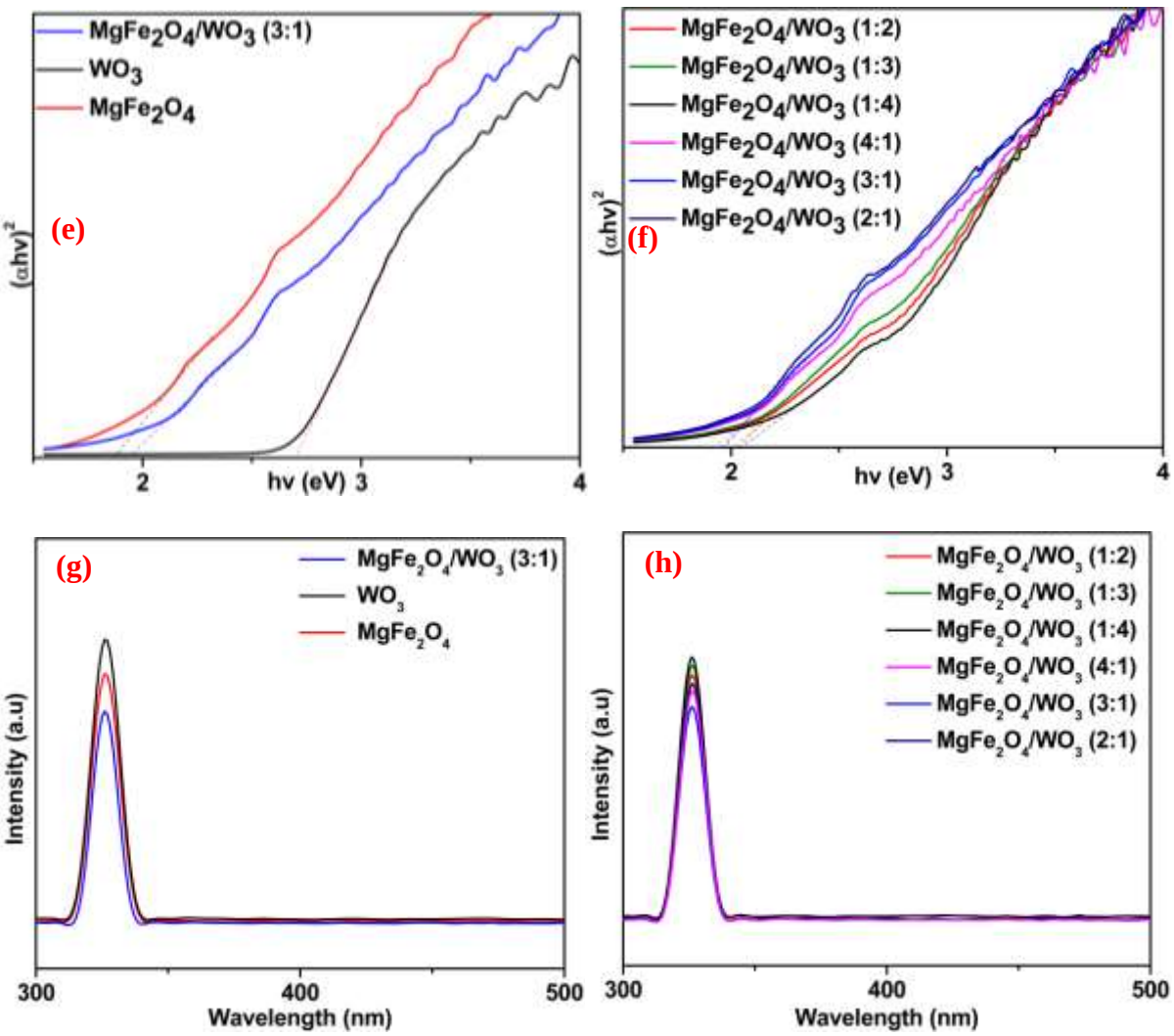

Figure 1. XRD (a-b), UV-Vis DRS (c-d), Tauc (e-f) and PL (g-h) of $MgFe_2O_4$, WO_3 and $MgFe_2O_4/WO_3$.

These results indicate that the materials are capable of generating electron–hole pairs under visible light irradiation. The positions of the conduction band (CB) and valence band (VB) are critical for the generation of reactive species. The CB of $MgFe_2O_4$ (-0.53 V vs. NHE) is more negative than the $O_2/O_2^{\bullet-}$ reduction potential (-0.33 V vs. NHE), enabling the reduction of O_2 to form $O_2^{\bullet-}$ [23]. Meanwhile, the VB of WO_3 (+3.31 V vs. NHE) is more positive than the $H_2O/HO^{\bullet}$ oxidation potential (+2.80 V vs. NHE), facilitating $HO^{\bullet}$ formation [24]. Therefore, the $MgFe_2O_4/WO_3$ composite can effectively utilize the CB of $MgFe_2O_4$ and the VB of WO_3 to generate $O_2^{\bullet-}$ and $HO^{\bullet}$ radicals, thereby enhancing its photocatalytic performance.

The PL spectra in Figure 1g–h reveal that all $MgFe_2O_4/WO_3$ composites with varying mass ratios exhibit significantly lower photoluminescence intensities compared to the individual $MgFe_2O_4$ and WO_3 samples. This decrease in PL intensity indicates a more effective suppression of e^-/h^+ recombination due to the synergistic interaction between the two components, thereby enhancing the photocatalytic performance of the composite materials. Notably, the $MgFe_2O_4/WO_3$ sample

with a 3:1 ratio shows the lowest PL intensity, suggesting superior photocatalytic activity. This finding will be further supported by the MB degradation results discussed in subsection 3.2. Based on the XRD, UV-Vis, and PL analyses, the $MgFe_2O_4/WO_3$ composite with 3:1 (wt./wt.) ratio was selected for further in-depth characterization, including SEM-EDX and FT-IR analyses.

Figure 2a–c illustrate the surface morphology of the samples, showing that $MgFe_2O_4$ consists of uniformly distributed spherical nanoparticles [26], while WO_3 exhibits a block-like structure with a smooth surface [27]. The $MgFe_2O_4/WO_3$ composite displays morphological features characteristic of both components, confirming their successful integration. The EDX spectrum (Figure 3a) reveals the elemental composition of the materials. For $MgFe_2O_4$, the presence of Mg (12.24 wt.%), Fe (63.71 wt.%), and O (24.05 wt.%) indicates high purity, with no impurities detected. Similarly, WO_3 consists of W (83.12 wt.%) and O (16.88 wt.%), also demonstrating high purity. In the $MgFe_2O_4/WO_3$ composite, the presence of Mg (8.44 wt.%), Fe (50.75 wt.%), O (21.48 wt.%), of the individuals, confirming the successful combination of both components and the high purity of the resulting material.

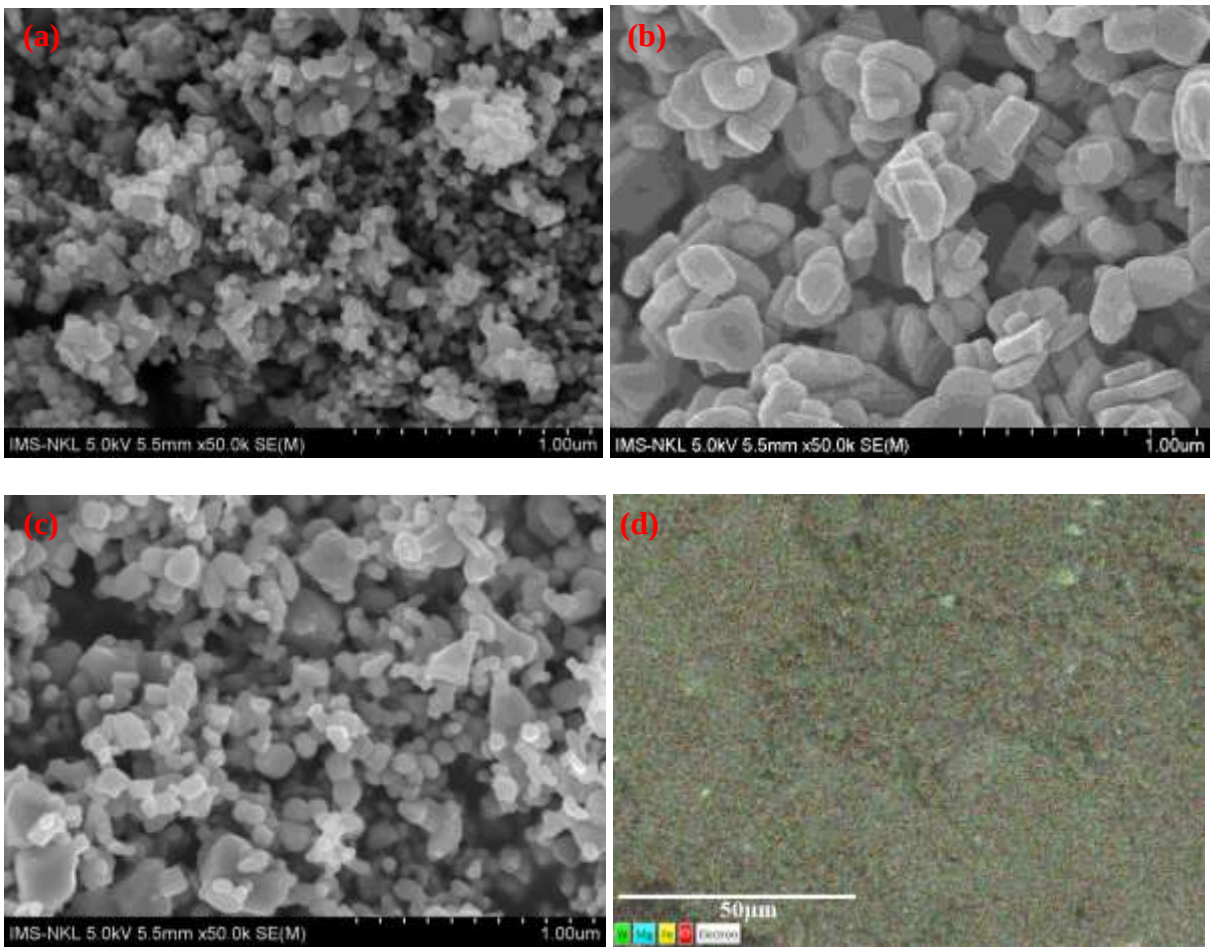

Figure 2. SEM of $MgFe_2O_4$ (a), WO_3 (b), $MgFe_2O_4/WO_3$ (c) and EDX- Mapping of $MgFe_2O_4/WO_3$ (d).

The FT-IR spectra in Figure 3b reveal the characteristic bonding features of $MgFe_2O_4$, WO_3, and the $MgFe_2O_4/WO_3$ heterostructure. The absorption bands at 450 cm^{-1} and 593 cm^{-1} correspond to the Mg–O and Fe–O vibrations in $MgFe_2O_4$ [18], respectively. For WO_3, the peak at 768 cm^{-1} is attributed to W=O stretching, while the band at 859 cm^{-1} corresponds to W–O–W bending vibrations [28]. Additionally, broad bands in the 3000–3700 cm^{-1} region are assigned to O–H stretching vibrations, likely due to surface-adsorbed water molecules 0. The $MgFe_2O_4/WO_3$ composite retains all the characteristic peaks of its individual components, confirming the successful formation of the composite material.

Based on the results of XRD, SEM, EDX, PL, and FT-IR analyses, it can be concluded that the $MgFe_2O_4/WO_3$ composite was successfully synthesized with high purity and a well-defined heterostructure. The XRD patterns confirm the coexistence of both crystalline phases of $MgFe_2O_4$ and WO_3, while SEM images show that the characteristic surface morphologies of the individual components are preserved in the composite. EDX analysis verifies the presence of Mg, Fe, W, and O elements without detectable impurities, indicating high material purity. The reduced PL intensity reflects effective suppression of electron–hole recombination, which contributes to enhanced photocatalytic performance. Furthermore, the FT-IR spectra confirm the presence of the characteristic bonds of both components in the composite. Altogether, these findings demonstrate the successful integration of $MgFe_2O_4$ and WO_3, forming a promising hetero-structured material for environmental remediation applications.

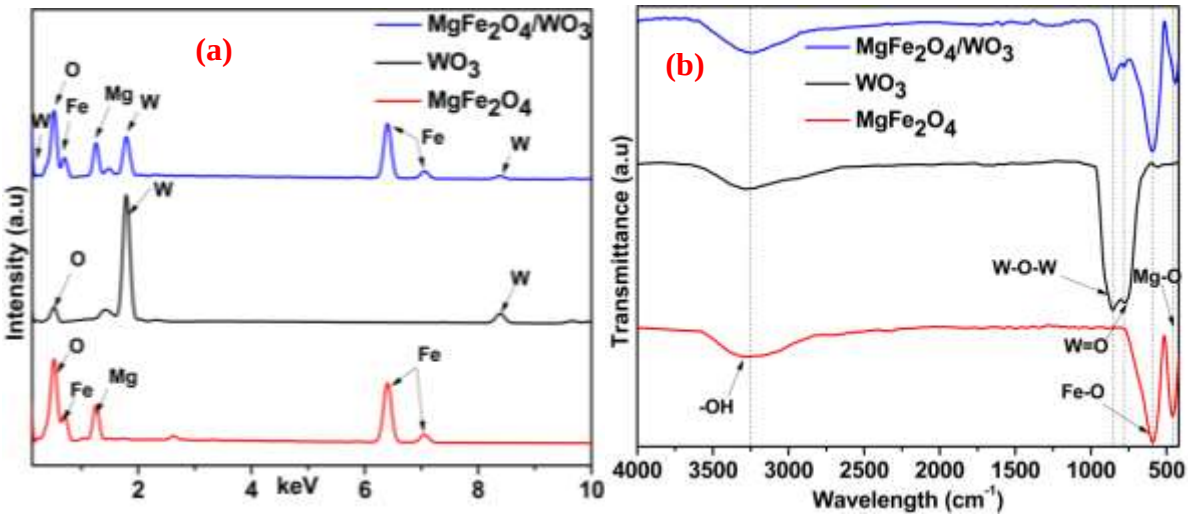

Figure 3. EDX (a) and FT-IR (b) of $MgFe_2O_4$, WO_3, $MgFe_2O_4/WO_3$.

3.2. Comparison of the Photocatalytic Performance of $MgFe_2O_4$, WO_3 and $MgFe_2O_4/WO_3$

To evaluate the photocatalytic performance of the produced materials, the degradation of MB was carried out using $MgFe_2O_4$, WO_3, and six $MgFe_2O_4/WO_3$ composites under identical conditions: pH 7.0, [MB] = 10 mg/L, catalyst dosage = 0.5 g/L, and a reaction time of 150 min. The composite samples had $MgFe_2O_4$:WO_3 mass ratios of 1:4, 1:3, 1:2, 2:1, 3:1, and 4:1, denoted as $MgFe_2O_4/WO_3$ (1:4) to $MgFe_2O_4/WO_3$ (4:1), respectively. As shown in Figure 4a, the individual components, $MgFe_2O_4$ and WO_3, achieved degradation efficiencies of only 46.91% and 28.78%, respectively. In contrast, all composite samples exhibited significantly improved performance, with

degradation efficiencies ranging from 62.25% to 78.55%. In which, The $MgFe_2O_4/WO_3$ (3:1) sample showed high degradation efficiency (76.73%) and the lowest e^-/h^+ recombination rate, indicating an optimal balance of light absorption and charge separation. Thus, it is a promising photocatalyst for treating organic pollutants in water.

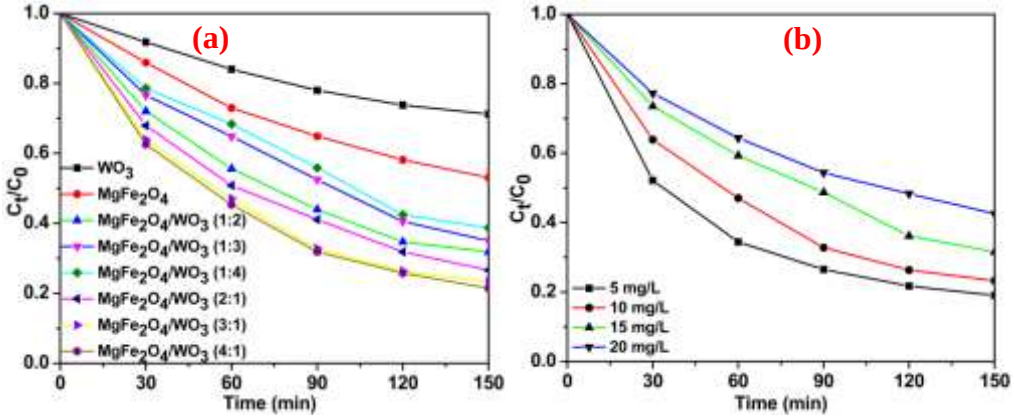

Figure 4. Comparison of MB degradation efficiency among $MgFe_2O_4$, WO_3, and various $MgFe_2O_4/WO_3$ ratios under the conditions: [Cat.] = 0.5 g/L, [MB] = 10 mg/L, pH 7.0 (a); and the effect of MB concentration on degradation efficiency at [Cat.] = 0.5 g/L, pH 7.0 (b).

3.3. Impact of MB Concentration

The effect of organic pollutant concentration was investigated using MB solutions with concentrations ranging from 5 to 20 mg/L. As shown in Figure 4b, the degradation efficiency gradually decreased with increasing pollutant concentration. The highest removal efficiency of 80.69% was achieved at the lowest MB concentration. However, when the MB concentration increased to 20 mg/L, the efficiency dropped to 57.43%. This decline can be attributed to the higher color intensity of the solution at elevated concentrations, which limits light penetration and subsequently reduces the generation of reactive species under illumination. Moreover, increasing the pollutant concentration while keeping the catalyst dosage constant leads to insufficient active sites on the photocatalyst surface, resulting in fewer radicals available to degrade the excess dye molecules, thus lowering the overall degradation performance [5, 9].

3.4. Kinetics of the Photodegradation Process

Three kinetics models were deployed to describe the degradation of MB in solution. The pseudo-zero-order, pseudo-1st-order, and pseudo-2nd-order kinetics can be written as follows:

$(C_0-C_t) = k_0 . t$

$-\ln C_0/C_t = k_1 . t$

$(C_0-C_t)/(C_0.C_t) = k_2 . t$

where k_0 ($mg.L^{-1}min^{-1}$), k_1 (min^{-1}), and k_2 ($L.min^{-1}.mg^{-1}$) are respectively the reaction rate constants for respective kinetics models.

Experimental results indicated that the degradation of MB followed the pseudo-second-order kinetics model most accurately (Figure 5a–c). The correlation coefficient (R^2) values for this model ranged from 0.9769 to 0.9987, significantly higher than those obtained from the pseudo-zero-order (R^2 from 0.5811 to 0.9035) and pseudo-first-order models (R^2 from 0.8660 to 0.9878). The reaction rate constant (k) for the pseudo-second-order model decreased as the initial MB concentration increased. Specifically, at 5 mg/L, the rate constant was 0.0058 $mg.L^{-1}.min^{-1}$, which decreased to 0.0005 $mg.L^{-1}.min^{-1}$ at 20 mg/L. Although the rate constant at 5 mg/L was notably higher than that at 10 mg/L, the overall degradation efficiency after 150 min was comparable (80.93% vs. 76.73%). Therefore, an

initial MB concentration of 10 mg/L is considered optimal for the photocatalytic degradation process. The durability and recovery of the catalyst and its application in wastewater samples will be conducted in our future studies to evaluate its application in real world wastewater treatment.

The outcomes of MB degradation obtained in this study are comparable and better than several photocatalysts previously reported. For instance, Barbosa et al., [7] reported a MB degradation efficiency of 83% by using $WO_3/CuWO_4$ heterojunction film, which is comparable to $MgFe_2O_4/WO_3$ in this work. However, $WO_3/CuWO_4$ heterojunction system requires 240 min to reach such an efficiency while $MgFe_2O_4/WO_3$ needs only 150 min. Similar studies on $MgFe_2O_4$ or WO_3 based photocatalyst also reported high degradation efficiencies for different types of organic dyes such as methyl orange (MO), direct blue 71 (DB-71), Rhodamine B (RhB) and malachite green [11-14]. These imply the potential application of $MgFe_2O_4/WO_3$ photocatalyst for the removal of organic pollutants in water.

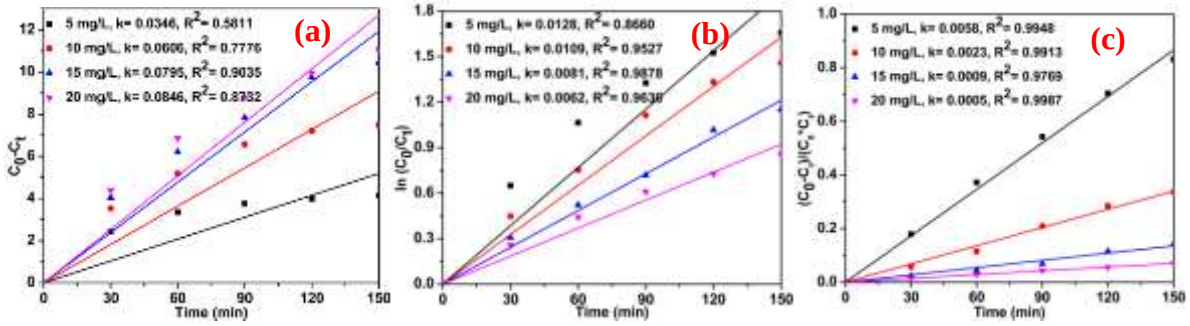

Figure 5. the pseudo-zero-order (a), pseudo-first-order (b), and pseudo-second-order kinetic models (c) of MB photodegradation process.

3.5. Mechanism of MB Degradation

The proposed mechanism for the photocatalytic degradation of MB using the $MgFe_2O_4/WO_3$ catalyst is illustrated in Figure 6 and described by Eqs (1–5). Under visible light irradiation, both $MgFe_2O_4$ and WO_3 absorb photons and generate e^-/h^+ pairs due to their suitable band gap energies. Subsequently, electrons from the conduction band (CB) of WO_3 transfer to the valence band (VB) of $MgFe_2O_4$. This charge transfer effectively suppresses the recombination of photogenerated electrons and holes. The electrons remaining in the CB of $MgFe_2O_4$ react with dissolved oxygen to produce $O_2^{\bullet-}$, while the holes in the VB of WO_3 can oxidize water molecules to generate $HO^{\bullet}$. These highly reactive oxygen species ($O_2^{\bullet-}$ and $HO^{\bullet}$) are primarily responsible for breaking down MB molecules into intermediate compounds and eventually converting them into harmless end-products such as CO_2 and H_2O [5, 7, 9, 14] (Figure 6).

The enhanced photocatalytic performance of the $MgFe_2O_4/WO_3$ composite can be attributed to the synergistic interaction between its two components, which allows for efficient utilization of the conduction and valence band potentials. This synergy minimizes charge recombination and promotes the generation of powerful oxidizing radicals, thereby accounting for the superior degradation efficiency observed with the $MgFe_2O_4/WO_3$ system.

$$MgFe_2O_4 + h\upsilon \rightarrow MgFe_2O_4^* (e^- + h^+) \quad (1)$$

$$WO_3 + h\upsilon \rightarrow WO_3^* (e^- + h^+) \quad (2)$$

$$O_2 + e^- \rightarrow O_2^{\bullet-} \quad (3)$$

$$h^+ + H_2O \rightarrow HO^{\bullet} \quad (4)$$

$$O_2^{\bullet-}, HO^{\bullet} + MB \rightarrow intermediates \rightarrow CO_2 + H_2O \quad (5)$$

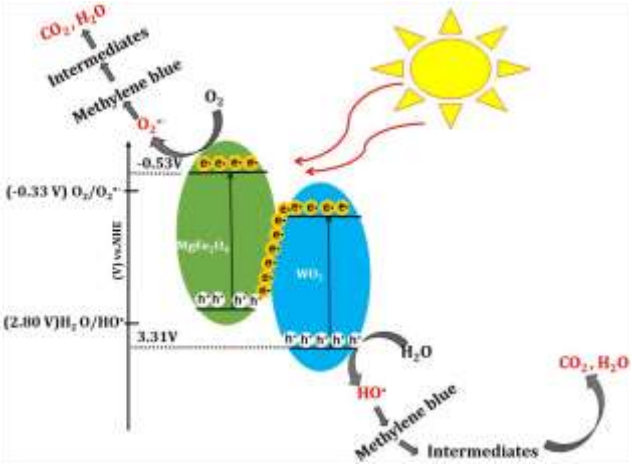

Figure 6. Photocatalytic mechanism of MB degradation using $MgFe_2O_4/WO_3$ photocatalyst.

4. Conclusion

In this study, a series of $MgFe_2O_4/WO_3$ composites with different mass ratios between two components were successfully synthesized, all exhibiting visible light-driven photocatalytic activity, with band gap energies ranging from 1.92 eV to 2.06 eV. The combination of $MgFe_2O_4$ and WO_3 significantly enhanced the photocatalytic efficiency by effectively suppressing the recombination of photogenerated electron–hole pairs. Among the produced materials, the composite with a 3:1 $MgFe_2O_4$ to WO_3 (mass ratio) demonstrated the most effective charge separation and the best photocatalytic performance. It was selected for further evaluation of the influence of various operational factors, including the initial pollutant concentration, on the photocatalytic activity. Under consistent reaction conditions (pH 7.0, catalyst dosage of 0.5 g/L, 10 mg/L MB solutions, and 150 min of visible light irradiation), the 3:1 $MgFe_2O_4/WO_3$ composite exhibited an MB degradation efficiency of bout 81%, meaning 1.64 times greater than pure $MgFe_2O_4$ and 2.67 times higher than pristine WO_3. The photocatalytic degradation followed the pseudo-second-order kinetics model while the MB degradation process was controlled by highly reactive oxygen species including $O_2^{\bullet-}$ and $HO^{\bullet}$. These results support the development of next-generation photocatalysts with high performance and practical applicability for wastewater treatment.

References

[1] Z. Li, H. Hanafy, L. Zhang, L. Sellaoui, M. S. Netto, M. L.S. Oliveira, M. K. Seliem, G. L. Dotto, A. B. Petriciolet, Q. Li, Adsorption of Congo Red and Methylene Blue Dyes on an Ashitaba Waste and a Walnut Shell-based Activated Carbon from Aqueous Solutions: Experiments, Characterization and Physical Interpretations, Chem. Eng. J, Vol. 388, 2020, pp. 124263, https://doi.org/10.1016/j.cej.2020.124263.

[2] A. I. L. Aguilar, A. M. T. Huerta, M. A. D. Crespo, M. L. X. N. Rodríguez, E. C. Barajas, S. B. B. Sibaja, A. E. R. Salazar, Valorization of Agroindustrial Orange Peel Waste during the Optimization of Activated Carbon–Multiwalled Carbon Nanotubes–Zinc Oxide Composites Used in the Removal of Methylene Blue in Wastewater, Chem. Eng. J, Vol. 492, 2024, pp. 152102, https://doi.org/10.1016/j.cej.2024.152102.

[3] P. E. Meissner, G. Mandi, B. Coulibaly, S. Witte, T. Tapsoba, U. Mansmann, J. Rengelshausen, W. Schiek, A. Jahn, I. Walter Sack, G. Mikus, J. Burhenne, K. D. Riedel, R. H. Schirmer, B. Kouyaté, O. Müller, Methylene Blue for Malaria in Africa: Results from a Dose-Finding Study in Combination with Chloroquine, Malar. J, Vol. 5, 2006, pp. 1-5, https://doi.org/10.1186/1475-2875-5-84.

[4] P. O. Oladoye, T. O. Ajiboye, E. O. Omotola, O. J. Oyewola, Methylene Blue Dye: Toxicity and Potential Elimination Technology from Wastewater, Results Eng, Vol. 16, 2022, pp. 100678, https://doi.org/10.1016/j.rineng.2022.100678.

[5] T. H. Le, D. T. Tran, T. P. T. Vu, L. D. Nghiem, A Novel Tertiary Magnetic $ZnFe_2O_4$/BiOBr/rGO Nanocomposite Catalyst for Photodegrading Organic Contaminants by Visible Light, Sci. Total Environ, Vol. 891, 2023, pp. 164358, https://doi.org/10.1016/j.scitotenv.2023.164358.

[6] D. T. Tran, T. T. U. Bui, A. T. Phan, T. B. Pham, Boosting Tetracycline Degradation by Integrating MIL-88A (Fe) with $CoFe_2O_4$ Persulfate Activators, Environ, Technol, Innov, Vol. 33, 2024, pp. 103502, https://doi.org/10.1016/j.eti.2023.103502.

[7] D. T. Tran, T. H. Nguyen, T. P.T. Vu, V. Q. Dang, T. T. T. Le, H. T. Van, Cu-ZnO/CdS/rGO Tertiary Heterojunction for Improved Photocatalytic Degradation of Synthetic Dyes Using Visible Light, J. Water Process Eng, Vol. 57, 2024, pp. 104687, https://doi.org/10.1016/j.jwpe.2023.104687.

[8] T. P. T. Vu, D. T. Tran, Q. T. Pham, Novel CdS/MIL-88A Heterojunction Coupled with H_2O_2/Air-Nanobubbles for Enhanced Visible-Light-Driven Photocatalytic Performance, J. Clean. Prod, Vol. 380, 2022, pp. 135007. https://doi.org/10.1016/j.jclepro.2022.135007.

[9] D. T. Tran, T. P. T. Vu, S. Kongmany, Accelerating Antibiotic Degradation by Integrating Tertiary Magnetic $ZnFe_2O_4$/$BiVO_4$/rGO Heterojunction with Ozone-Nanobubbles, Chem. Eng. J, Vol. 494, 2024, pp. 153306, https://doi.org/10.1016/j.cej.2024.153306.

[10] R. M. Surya, Y. Yulizar, A. H. Cahyana, D. O. B. Apriandanu, One-Pot Cajanus cajan (L.) Millsp. Leaf Extract-Mediated Preparation of $MgFe_2O_4$ Nanoparticles: Optical, Structural, Morphological and Particle Size Analyses, Solid State Commun, Vol. 326, 2021, pp. 114170, https://doi.org/10.1016/j.ssc.2020.114170.

[11] A. Kiani, G. Nabiyouni, S. Masoumi, D. Ghanbari, A Novel Magnetic $MgFe_2O_4$–$MgTiO_3$ Perovskite Nanocomposite: Rapid Photo-Degradation of Toxic Dyes under Visible Irradiation, Compos. B: Eng, Vol. 175, 2019, pp. 107080, https://doi.org/10.1016/j.compositesb.2019.107080.

[12] N. R . Su, P. Lv, M. Li, X. Zhang, M. Li, J. Niu, Fabrication of $MgFe_2O_4$–ZnO Heterojunction Photocatalysts for Application of Organic Pollutants, Mater. Lett. Vol. 122, 2014, pp. 201-204, https://doi.org/10.1016/j.matlet.2013.12.106.

[13] J. Jia, X. Du, Q. Zhang, E. Liu, J. Fan, Z-scheme $MgFe_2O_4$/Bi_2MoO_6 Heterojunction Photocatalyst with Enhanced Visible Light Photocatalytic Activity for Malachite Green Removal, Appl. Surf. Sci, Vol. 492, 2019, pp. 527-539, https://doi.org/10.1016/j.apsusc.2019.06.258.

[14] T. P. T. Vu, D. T. Tran, V. C. Dang, Novel N,C,S-TiO_2/WO_3/rGO Z-scheme Heterojunction with Enhanced Visible-Light Driven Photocatalytic Performance, J. Colloid Interface Sci, Vol. 610, 2021, pp. 49-60, https://doi.org/10.1016/j.jcis.2021.12.050.

[15] L. Cheng, Y. Zhang, W. Fan, Y. Ji, Synergistic Adsorption Photocatalysis for Dyes Removal by a Novel Biochar-Based Z-Scheme Heterojunction BC/2ZIS/WO_3: Mechanistic Investigation and Degradation Pathways, Chem. Eng. J, Vol. 445, 2022, pp. 136677, https://doi.org/10.1016/j.cej.2022.136677.

[16] M. B. Tahir, Microbial Photoelectrochemical Cell for Improved Hydrogen Evolution Using Nickel Ferrite Incorporated WO_3 under Visible Light Irradiation, Int. J. Hydrog. Energy, Vol. 44, 2019, pp. 17316-17322, https://doi.org/10.1016/j.ijhydene.2019.01.067.

[17] M. L. Barbosa, M. J. S. Costa, A. E. B. Lima, A. M. Batista, E. Longo, R. S. Cavalcante, L. S. Santos, Anionic and Cationic Dyes Removal by Degradation via Photoelectrocatalysis Using a WO_3/$CuWO_4$ Heterojunction Film as a Photoanode, Nano-Struct. Nano-Objects, Vol. 35, 2023, pp. 100993, https://doi.org/10.1016/j.nanoso.2023.100993.

[18] D. T. Tran, T. D. To, T. H. Le, Q. T. Dao, L. D. Nghiem, Synthesis of Highly Effective and Easily Recoverable MIL-100(Fe)/$MgFe_2O_4$ Adsorbent for Enhanced Antibiotic Removal from Water, J. Ind. Eng. Chem, Vol. 147, 2025, pp. 149-160, https://doi.org/10.1016/j.jiec.2024.12.009.

[19] T. N. Anh, N. T. Hien, V. T. Tran, D. T. H. Linh, N. T. Hanh, L. T. Do, N. H. Vu, N. M. Hoang, D. V. Quang, D. V. Dao, 92.58% Efficiency of Solar-Driven Degradation of Tetracycline Solution by Pt/WO_3 Nanohybrid, Inorg. Chem. Commun, Vol. 161, 2024, pp. 112100, https://doi.org/10.1016/j.inoche.2024.112100.

[20] B. R. Thombare, P. R. Dusane, P. K. Bankar, G. S. Lole, A. B. Deore, C. V. Khedkar, P. S.

Badgujar, D. S. Gavhane, M. A. More, S. I. Patil, Photoelectron Properties and Enhanced Field Electron Emission of Cobalt Ferrite Reduced Graphene Oxide Nanocomposite, J. Electron Spectrosc. Relat. Phenom, Vol. 260, 2022, pp. 147245, https://doi.org/10.1016/j.elspec.2022.147245.

[21] D. T. Tran, V. N. Nguyen, rGO Persulfate Metal Free Catalytic System for the Degradation of Tetracycline: Effect of Reaction Parameters, Mater. Res. Express, Vol. 7, 2020, pp. 075501, https://doi.org/10.1088/2053-1591/ab9e47.

[22] D. T. Tran, T. H. Nguyen, T. H. Doan, V. C. Dang, L. D. Nghiem, Removal of Direct Blue 71 and Methylene Blue from Water by Graphene Oxide: Effects of Charge Interaction and Experimental Parameters, J. Dispers. Sci. Technol, Vol. 44, 2022, pp. 2508-2519, https://doi.org/10.1080/01932691.2022.2102034.

[23] K. M. Katubi, A. Murtaza, H. M. Asif, Z. A. Alrowaili, M. S. Al Buriahi, S. Munir, M. F. Warsi, Fabrication and Characterization of Ternary Composite $MgFe_2O_4/MoO_3$@CNTs for the Enhanced Photocatalytic Activity to Degrade Organic Pollutants, J. Alloys Compd, Vol. 978, 2024, pp. 173327, https://doi.org/10.1016/j.jallcom.2023.173327.

[24] T. A. T. Do, D. T. Nguyen, T. G. Ho, H. T. Giang, Q. N. Pham, T. H. L. Nghiem, T. H. Nguyen, M. T. Man, Mechanism of Simultaneous Photocatalytic Degradation of Rhodamine B and Cr(VI) under Visible Light Using WO_3 Nanotubes, Adv. Nat. Sci: Nanosci. Nanotechnol, Vol. 15, 2024, pp. 015010, https://doi.org/10.1088/2043-6262/ad2c7f.

[25] N. Moghni, H. Boutoumi, H. Khalaf, N. Makaoui, G. Colón, Enhanced Photocatalytic Activity of TiO_2/WO_3 Nanocomposite from Sonochemical Microwave Assisted Synthesis for the Photodegradation of Ciprofloxacin and Oxytetracycline Antibiotics under UV and Sunlight, J. Photochem. Photobiol. A Chem, Vol. 428, 2022, pp. 113848, https://doi.org/10.1016/j.jphotochem.2022.113848.

[26] J. Zhang, M. Yan, G. Sun, X. Li, K. Liu, Visible Light Photo Fenton Catalytic $MgFe_2O_4$ Spinel: Reaction Sintering Synthesis and DFT Study, J. Alloys Compd, Vol. 889, 2021, pp. 161673, https://doi.org/10.1016/j.jallcom.2021.161673.

[27] F. Peng, S. Wang, W. Yu, T. Huang, Y. Sun, C. Cheng, X. Chen, J. Hao, N. Dai, Ultrasensitive ppb-Level H_2S Gas Sensor at Room Temperature Based on WO_3/rGO Hybrids, J. Mater. Sci.: Mater. Electron, Vol. 31, 2020, pp. 5008-5016, https://doi.org/10.1007/s10854-020-03067-6.

[28] R. Justinabraham, A. Durairaj, S. Vasanthkumar, Preparation of a Silver Ferrite Assisted Tungsten Oxide Nanocomposite for Efficient Sonocatalytic Degradation of Organic Pollutants Activated by PMS Followed by Toxicity Evaluation, New J. Chem, Vol. 48, 2024, pp. 4482-4495, https://doi.org/10.1039/D4NJ00390J.

[29] S. H. Baek, J. Yun, S. H. Lee, H. W. Lee, Y. Kwon, K. R. Park, Y. Song, B. S. Kim, R. Kwak, H. Hwang, D. W. Jeong, Real Time Analysis and Prediction Method of Ion Concentration Using the Effect of O-H Stretching Bands in Aqueous Solutions Based on ATR-FTIR Spectroscopy, RSC Adv, Vol. 14, 2024, pp. 20073-20080, https://doi.org/10.1039/D4RA01473A.